



Temporal walk-off induced dissipative quadratic solitons

Arkadev Roy¹, Rajveer Nehra¹, Saman Jahani¹, Luis Ledezma¹, Carsten Langrock², Martin Fejer² and Alireza Marandi¹✉

A plethora of applications have recently motivated extensive efforts regarding the generation of Kerr solitons and coherent frequency combs. However, the Kerr (cubic) nonlinearity is inherently weak. By contrast, strong quadratic nonlinearity in optical resonators is expected to provide a promising alternative means for soliton formation. Here we demonstrate dissipative quadratic soliton formation via non-stationary optical parametric amplification in the presence of pronounced temporal walk-off between pump and signal, leading to half-harmonic generation accompanied by a substantial pulse compression (exceeding a factor of 40) supported at low pump pulse energies (~4 pJ). The quadratic soliton forms in a low-finesse cavity in both normal and anomalous dispersion regimes. We present a route to considerably improve the performance of the demonstrated quadratic soliton when extended to an integrated platform to realize highly efficient extreme pulse compression, leading to the formation of few-cycle soliton pulses starting from ultra-low-energy picosecond-scale pump pulses.

The formation of dissipative solitons in nonlinear resonators has become a versatile mechanism for stable femtosecond sources^{1,2}. In the frequency domain it corresponds to a broadband frequency comb, which, when self-referenced, leads to a myriad of applications in precision measurements, including spectroscopy^{3,4}, astro-combs^{5,6}, atomic clocks⁷, ranging^{8,9} and imaging¹⁰, to name a few. Recently, the ambit of frequency combs has expanded to cover promising avenues such as massively parallel data communication¹¹ and the realization of machine learning accelerators¹². To cater to this increasing list of technologically important applications there are a number of outstanding challenges to be addressed, including attaining low-power operation¹³, high pump-to-soliton conversion efficiency^{14–18}, broadband (octave-spanning and widely tunable) comb formation in a compact platform^{19,20}, reliable fabrication and operation of high-Q resonators.

In the past decade there has been extensive research on Kerr-based frequency combs where a $\chi^{(3)}$ nonlinear resonator is coherently driven by a continuous-wave (c.w.) laser to excite temporal solitons². However, the Kerr nonlinearity, being a cubic nonlinearity, is inherently weak, and so requires the use of high-Q resonators to reach the threshold of parametric oscillation with reasonable pump power. The frequency comb forms around the driving c.w. laser, and it requires precise dispersion engineering and, in some cases, the use of multiple pump lasers²¹ to extend the comb to its harmonics and sub-harmonics. These issues can be alleviated by operating with quadratic nonlinearity, which can typically cause substantial nonlinear mixing at power levels that are orders of magnitude lower than its cubic counterpart²². With the ability to perform harmonic conversion through properly phase-matched quadratic nonlinear interactions, $\chi^{(2)}$ nonlinear media promise an ideal platform to realize widely tunable self-referenced frequency combs. Although frequency comb generation through quadratic nonlinearity^{23–28} and femtosecond optical parametric oscillators²⁹ has been the subject of several theoretical and experimental investigations, demonstrations of quadratic soliton formation remain rare^{22,30}.

Fundamental limits on the efficiency (pump-to-soliton conversion) of c.w.-pumped Kerr solitons^{15,16} have motivated study of their pulsed-pump-driven arrangements^{6,17}. Modulated pumps also provide additional control on the dynamics of the temporal solitons^{31–33}. Another route to achieve high conversion efficiency is to use low-finesse cavities with large outcoupling, where the roundtrip loss is compensated by proportionate amplification³⁴. Thus, soliton formation in a synchronously pumped low-finesse quadratic nonlinear resonator represents a viable route to realize highly efficient and widely tunable broadband frequency combs³⁰.

In this Article we demonstrate walk-off-induced temporal solitons in a degenerate optical parametric oscillator (OPO) based on pure quadratic nonlinearity. We follow the notion of the dissipative solitons as defined in ref. ³⁵. We show that the quadratic soliton can be supported in both normal and anomalous group-velocity dispersion regimes. We also show that this quadratic soliton exists in a low-finesse optical cavity, which can lead to high conversion efficiency. We achieve giant pulse compression exceeding a factor of 40 at picojoule-level pump energy. We investigate the dynamics of this quadratic soliton and characterize its different regimes of operation. Furthermore, we define a figure of merit (FOM) that can act as the design guideline for achieving extreme pulse compression and optimum soliton formation in a dispersion-engineered cavity that can be accessible through integrated platforms. Our results pave the way for the generation of energy-efficient dissipative quadratic solitons, breaking some of the barriers for the generation of Kerr solitons, which demand high-Q cavities, feature-limited conversion efficiency and anomalous dispersion for bright soliton formation and possess limited wavelength tunability.

Results

We consider a degenerate OPO³⁶, as illustrated in Fig. 1a (a detailed schematic is provided in Supplementary Section 2). The OPO is driven synchronously by a pump pulse with a temporal width of several picoseconds. The quadratic nonlinear interaction takes place in a periodically poled lithium niobate waveguide^{37,38},

¹Department of Electrical Engineering, California Institute of Technology, Pasadena, CA, USA. ²Edward L. Ginzton Laboratory, Stanford University, Stanford, CA, USA. ✉e-mail: marandi@caltech.edu

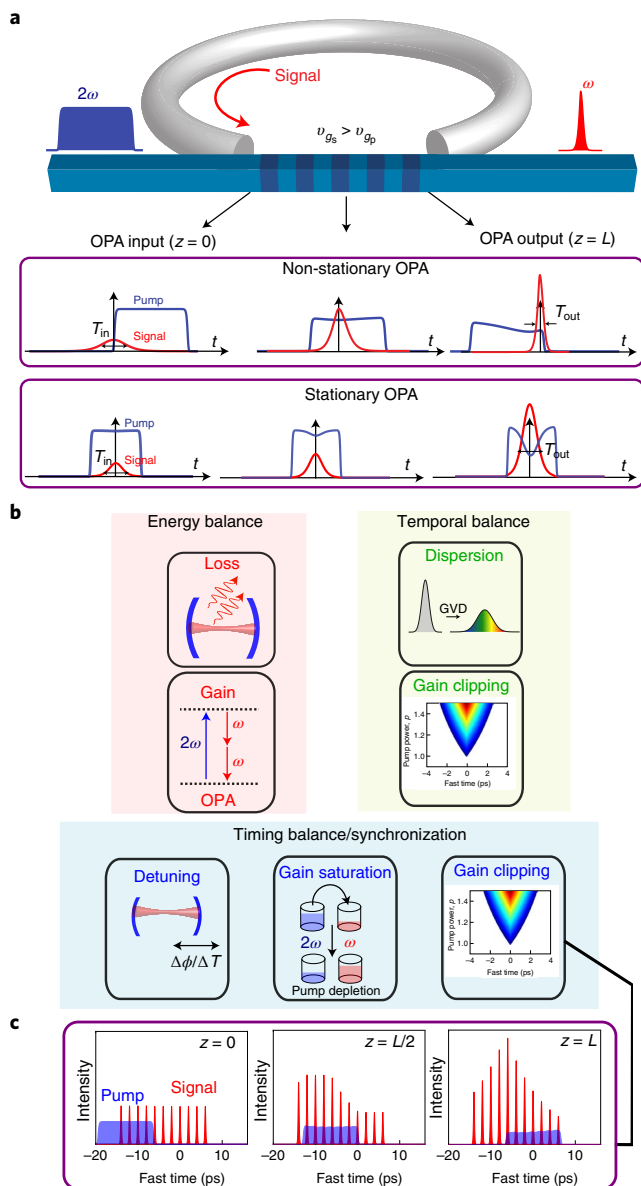


Fig. 1 | Walk-off-induced quadratic soliton formation process.

a, Schematic of the doubly-resonant half-harmonic synchronously pumped OPO with resonant signal and non-resonant pump. The quadratic nonlinear interaction takes place in the periodically poled region and, owing to the large GVM between the signal (v_{gs} is the signal group velocity) and the pump (v_{gp} is the pump group velocity), substantial pulse compression occurs due to the non-stationary OPA process as the signal walks off (along the propagation direction z) through the pump. This is contrasted with the stationary OPA case, which features negligible temporal walk-off, and the signal amplification is not accompanied by considerable pulse compression. **b**, The dissipative soliton is sustained in the OPO by a triple balance of energy, temporal broadening and timing. The energy loss through dissipation is balanced by the parametric gain through the OPA process, whereas the temporal broadening due to the group-velocity dispersion is arrested by the temporal gain-clipping mechanism. Finally, timing synchronization is achieved by the delicate balance between linear cavity detuning, nonlinear acceleration due to gain saturation and the gain-clipping mechanism. **c**, Illustration of the temporal gain-gating mechanism, that is, the dependence of gain on the relative delay between the pump and signal pulses, which is responsible for the gain clipping. The signal pulse that experiences maximum temporal overlap with the pump pulse throughout the non-stationary OPA process extracts the highest gain.

providing parametric interactions between the pump at the fundamental frequency and the signal at the half-harmonic frequency. The cavity is completed with a combination of polarization-maintaining fibres and a suitable free-space section to ensure that the pump repetition rate is approximately equal to multiples of the cavity free spectral range.

The walk-off-induced quadratic soliton formation is supported by a non-stationary optical parametric amplification (OPA) process^{39,40}. The temporal soliton at the half-harmonic (1,550 nm) walks through the pump (775 nm) due to the group-velocity mismatch (GVM; Supplementary Section 3). This allows a signal pulse that is much shorter than the pump pulse to extract most of the pump energy. By contrast, in a stationary OPA process (with negligible temporal walk-off between the pump and signal), the signal is amplified without considerable pulse compression, as shown in Fig. 1a⁴¹. Figure 1b shows the mechanisms contributing to the non-linear dynamics of the OPO that are responsible for this quadratic soliton formation. The dissipative soliton loses energy via different dissipation pathways of the low-finesse cavity, which include intrinsic cavity roundtrip loss and the outcoupling. This energy loss is counterbalanced by the parametric amplification process. The OPO oscillation threshold occurs when the parametric gain overcomes the loss, and the quadratic soliton is supported near threshold.

The group-velocity dispersion (GVD) of the medium (waveguide+cavity) leads to temporal pulse broadening. This GVD-induced broadening is prevented by the temporal gain-clipping mechanism (Supplementary Section 3)³⁶. The pulsed pumping scheme in the synchronously driven OPO leads to a temporal gain window that is responsible for the time gating of the parametric gain and is expressed by the gain-clipping effect. In Fig. 1c we consider the unsaturated amplification of several signal pulses with different temporal positions on a fast timescale with respect to the pump pulse. The signal pulse that undergoes maximal overlap with the pump in the entire non-stationary OPA process experiences the maximum gain. This gain gradually decreases on either side of this optimal temporal position on the fast-time axis, thereby enforcing a temporal gating of the gain. This gain window progressively broadens as the pump power is increased above threshold. A signal pulse that experiences GVD-induced temporal broadening and extends beyond this temporal gain window will experience less net gain. This competition between GVD and the gain-clipping mechanism gives rise to the temporal balance.

Finally, the timing balance (synchronization) is determined by the mutual interplay between the linear cavity detuning, gain saturation and the gain clipping. The cavity detuning causes a timing mismatch from exact synchrony with the pump repetition rate. Doubly-resonant OPOs can only oscillate around cavity detunings where the roundtrip phase accumulations are integer multiples of π (ref. 36). The cavity detuning phase can be expressed as $\Delta\phi = \pi l$, where integer values of l represents the centre of these discrete OPO peaks, as shown in Fig. 2a,b. A magnified view of a single peak structure is shown in the inset of Fig. 2a. Within a peak, the OPO can oscillate in degenerate or non-degenerate regimes⁴². We operate at the cavity detuning that corresponds to the degenerate mode of operation to access the dissipative quadratic soliton. The timing mismatch (detuning-induced delay with respect to the synchronous pumping) can be expressed as $\Delta T = \frac{\lambda l}{2c}$, where c is the group velocity of the half-harmonic signal with wavelength λ in the cavity.

The gain saturation arises due to the pump depletion. As the signal walks through the pump (due to the GVM), the leading edge of the soliton experiences larger gain than the trailing edge, because the trailing edge experiences the depleted pump. This causes a pulse centroid shift in response to this underlying nonlinear acceleration³⁰. The gain clipping, on the other hand, is aligned with the pump temporal position on the fast timescale and also contributes to the timing balance. The synchronization of the quadratic soliton supported in

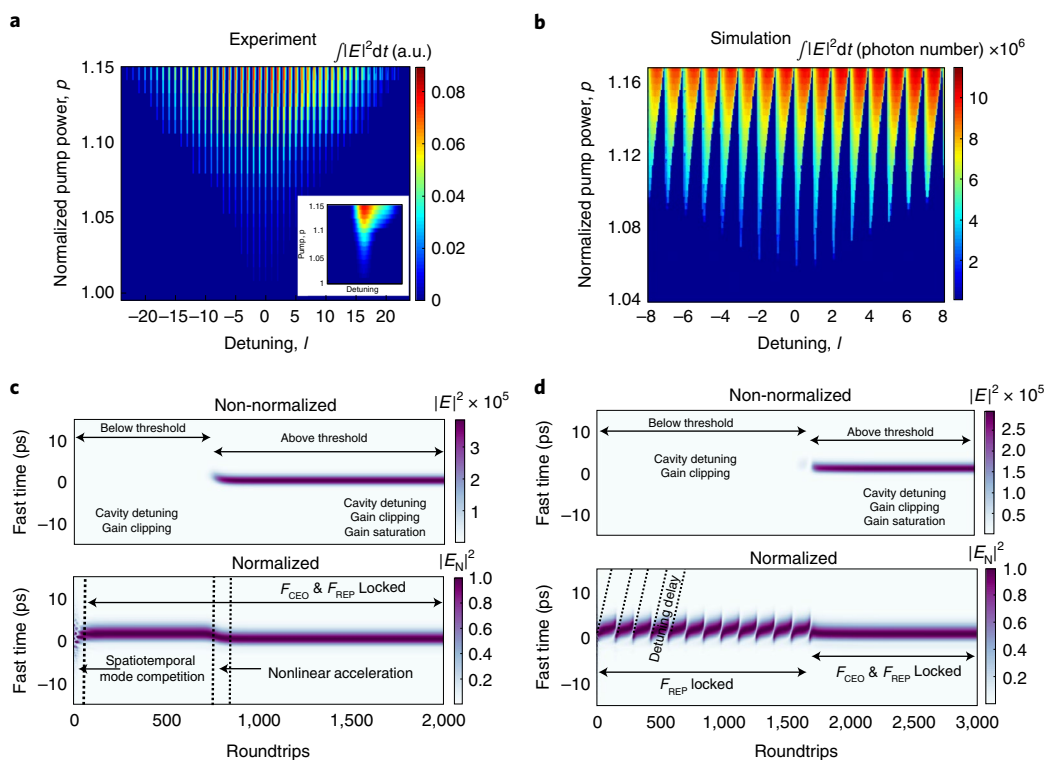


Fig. 2 | Cavity detuning dependence of doubly-resonant OPO and its impact on synchronization. **a, b**, Mode-locking range of doubly-resonant sync-pumped OPO as a function of cavity detuning obtained experimentally (**a**) and via numerical simulation (**b**). OPO oscillation occurs around discrete peaks centred at integer values of detuning parameter l . A zoomed view of a single peak is shown in the inset of **a**. **c**, Evolution of the intra-cavity OPO field from random noise to the approximate sech-shaped signal soliton pulses in the steady state. Top: non-normalized intensity. Bottom: normalized intensity to highlight the different dynamical regimes. **d**, Evolution of the intra-cavity OPO field in the case of large cavity detuning ($l=50$), highlighting the importance of gain saturation and gain clipping in timing balance and synchronization. Top: non-normalized intensity. Bottom: normalized intensity to highlight the different synchronization regimes in the large detuning scenario.

the synchronously pumped OPO can be expressed in terms of F_{CEO} (carrier envelope offset frequency) locking and F_{REP} (repetition frequency) locking to the pump. Although the doubly-resonant OPO can have multiple modes of operation (Supplementary Section 8), the quadratic soliton in the steady state exists in the F_{REP} and F_{CEO} locked synchronized state. The demonstrated quadratic soliton is thus capable of transferring the frequency comb stability properties of the pump in addition to the coherent spectral broadening (the pulse shortening) mechanism. The spontaneous evolution of these solitonic pulses from background noise obtained via numerical simulation is shown in Fig. 2c. The non-normalized version (top panel, Fig. 2c) and normalized version (bottom panel, Fig. 2c, where the intra-cavity intensity of each roundtrip is normalized to itself) of the roundtrip evolution highlight the several dynamical regimes of the quadratic soliton formation. The nonlinear dynamics is initiated by spatiotemporal gain competition, followed by gradual building up of the signal/soliton pulse, which eventually becomes intense enough to undergo gain saturation, leading to pulse centroid shift and nonlinear acceleration. Finally, the soliton reaches the steady state and maintains synchronization with the pump. Figure 2d shows the time evolution of the OPO in the case of large cavity detuning. This exemplifies the role of gain saturation and gain clipping in timing balance and synchronization. Large cavity detuning is also associated with timing mismatch (from exact synchrony), which results in a pulse delay or advance each roundtrip, as shown in the initial evolution cycles in the bottom panel of Fig. 2d. The slope of this pulse delay is represented by the dotted lines and corresponds to the cavity detuning-induced timing delay (ΔT). Below threshold, this large timing mismatch cannot be completely compensated by the

gain-clipping mechanism, leading to an F_{CEO} unlocked state, with the signal still maintaining F_{REP} locking. Above threshold, onset of gain saturation takes place, and the combined effect of gain saturation and gain clipping leads to the timing balance resulting in the soliton maintaining synchronization (F_{CEO} and F_{REP} locked) with the pump. The combination of these balancing effects can be elucidated using the semi-analytical variational formalism, which expresses the pulse parameters (energy, temporal width and centroid) in terms of the cavity and driving parameters (Supplementary Section 3.2)³⁶.

Figure 3 shows the measured and simulated spectral and temporal characteristics of the quadratic soliton. Substantial spectral broadening of the signal compared to the pump is shown in Fig. 3a,b. The soliton pulse is characterized using an intensity cross-correlation technique as shown in Fig. 3c overlaid with the pump pulses at the output of the waveguide. The OPO operation at degeneracy is confirmed by the radiofrequency beat-note measurement (Supplementary Section 5).

The quadratic soliton is formed near the oscillation threshold of the OPO. The OPO threshold is associated with a phase transition in the spatiotemporal correlation properties of the quadrature fluctuations and the accompanying symmetry breaking⁴³. As the pump power (expressed in normalized p , denoting the number of times above threshold) increases further above threshold, the temporal width of the gain-clipping region increases, and the soliton transitions into the box-pulse regime (Supplementary Section 4)³⁶. In the box-pulse regime, gain clipping dominates over the cavity GVD, and the pulse assumes a box-pulse shape, deviating from the approximate sech profile in the near-threshold soliton regime. In the soliton regime, the effect of GVD is counterbalanced by the gain

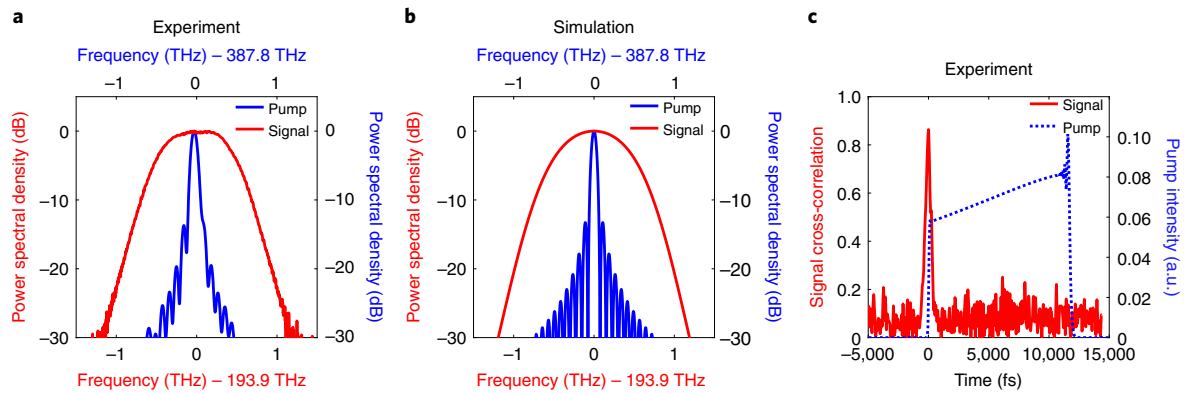


Fig. 3 | Spectral and temporal characteristics of the quadratic soliton. **a, b**, Spectrum of the soliton (the signal at the half-harmonic centred around 193.9 THz is represented by a red solid line) obtained experimentally (**a**) and through numerical simulation (**b**). The pump spectrum is represented by blue solid lines centred around 387.8 THz. **c**, The degenerate half-harmonic quadratic soliton formation is accompanied by substantial temporal pulse compression, as can be visualized from the intensity cross-correlation trace. The flat-top pump temporal profile (-13.2 ps) is shown as a blue dotted line and is obtained by numerical simulation.

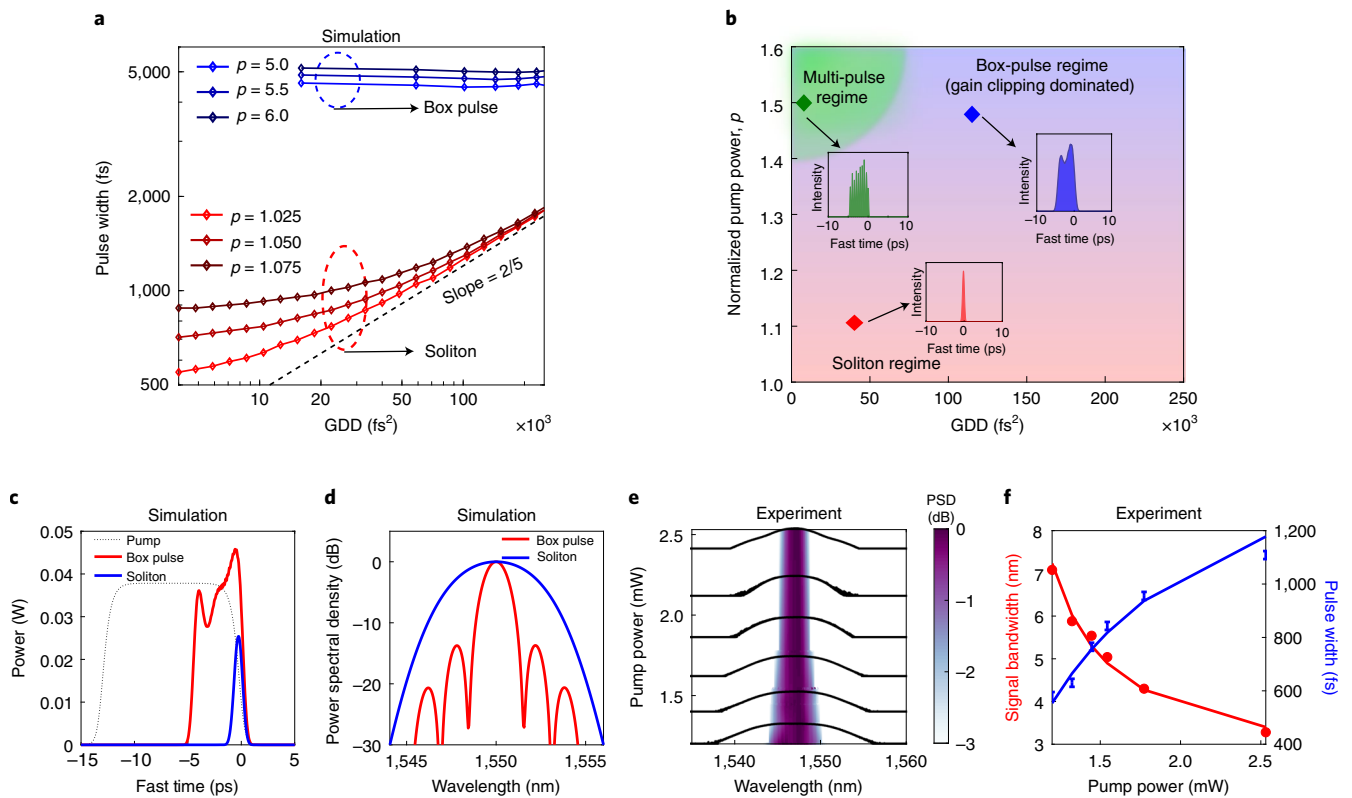


Fig. 4 | Soliton and box-pulse regimes. **a**, Pulse width scaling as a function of dispersion in the soliton and box-pulse regimes. The soliton pulse width scales linearly (in log scale) with dispersion, whereas the pulse width in the box-pulse regime, which is dominated by gain clipping, is almost independent of dispersion. **b**, Illustrative phase diagram in the parameter space of pump power and dispersion, indicating the regions of existence of various pulse regimes (soliton, box-pulse and multi-pulse). **c, d**, Temporal profiles (**c**) and spectrum (**d**) of the OPO in the soliton and box-pulse regimes, respectively. The doubly-resonant OPO supports the quadratic soliton near threshold, and it transits to box-pulse-shaped pulses as the pump power is raised above threshold. **e**, Spectral narrowing as the OPO enters further into the box-pulse regime, as is evident from the decreasing OPO 3-dB bandwidth. The shading represents the 3-dB portion of the spectra (PSD, power spectral density). **f**, The associated temporal broadening reflected in terms of temporal full-width at half-maximum obtained from the intensity cross-correlation data as the pump power is increased above threshold. The solid curves represent fits according to the gain-clipping variation. The error bars represent uncertainty associated with the intensity cross-correlation technique.

clipping, and the soliton exhibits characteristic pulse-width variation with a power-law dependence on the total cavity dispersion (group delay dispersion, GDD; scaled to the $2/5$ power of the GDD, Supplementary Section 3.2), while in the box-pulse regime the pulse

length is almost invariant with GDD. This distinct pulse-width scaling is shown in Fig. 4a. Figure 4b presents an illustrative diagram of the region of the existence of different pulse regimes in the parameter space of pump power and dispersion. The soliton

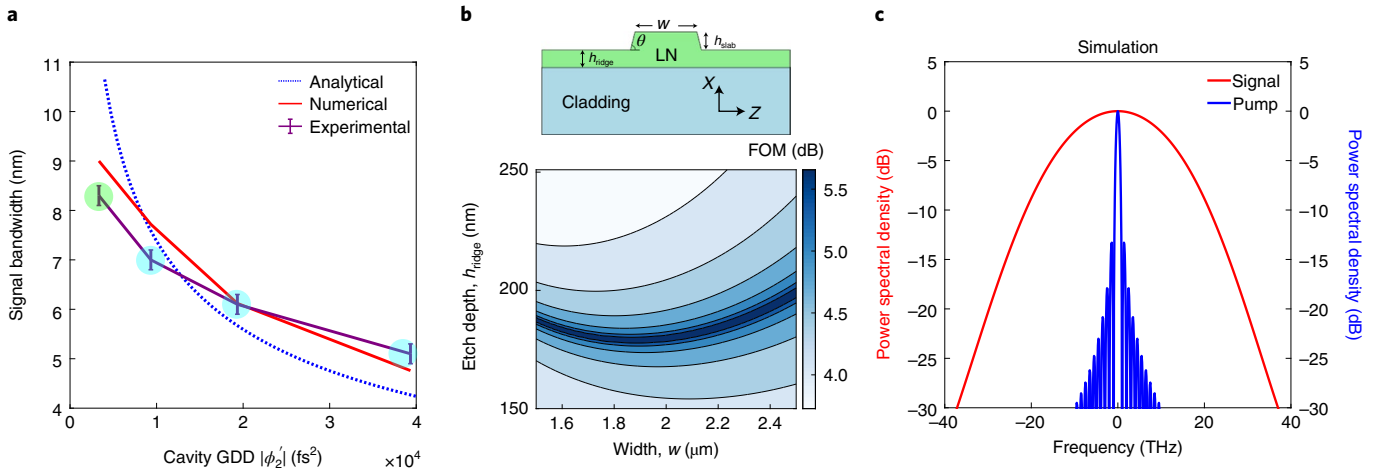


Fig. 5 | Dispersion engineering and efficient half-harmonic soliton pulse compression. **a**, Variation of the soliton bandwidth as a function of cavity dispersion. Different dispersion configurations are realized in the experiment by altering the combination of normal- (dispersion-compensating polarization-maintaining fibres) and anomalous dispersion (polarization-maintaining fibres) fibres. The blue and green circles refer to scenarios corresponding to net normal and net anomalous cavity dispersion, respectively. The error bars represent variations due to uncertainty in the number of times above threshold operation in different GDD scenarios. **b**, Fine control in the dispersion engineering is possible in thin-film integrated waveguide-based devices by choosing appropriate etch depth and waveguide width. The FOM defined in equation (1) is plotted, where high values of FOM indicate large attainable pulse compression. Here, L is assumed to be 6 mm. **c**, Numerical simulation corresponding to the optimum FOM, showing notable spectral broadening in soliton formation, corresponding to pulse compression by a factor of ~ 60 .

regime is accessed close to threshold. When the pump power is far above threshold, the system enters the box-pulse regime for large values of dispersion, whereas multi-pulsing occurs for small values of dispersion. Typical spectral and temporal characteristics of the OPO in the solitonic and box-pulse regimes are shown in Fig. 4c,d. The 3-dB spectral bandwidth of the OPO decreases with increasing pump power, as shown in Fig. 4e, and the corresponding variation of the measured full-width at half-maximum of the pulses in the time domain is shown in Fig. 4f. This scaling of the pulse width is distinct from the temporal solitons, which are bright/dark soliton pairs in a quadratic medium (Supplementary Section 11)⁴⁴.

The soliton pulse width can be obtained from semi-analytical variational calculations (Supplementary Section 3), and its dependence on the cavity parameters can be expressed as

$$\tau_{\text{sech}} = \left(\frac{7}{15} \frac{(\phi_2')^2 T_p}{\ln(G_0) \ln(2)} \right)^{\frac{1}{5}},$$

where ϕ_2' is the cavity GDD, $(1 - G_0^{-1})$ represents the roundtrip loss, and T_p is the pump pulse width. We have assumed the optimum pump pulse width ($T_p = Lu$, where L is the waveguide length and u is the walk-off parameter) where the pulse width matches the walk-off length in the waveguide (Supplementary Section 9). Also, the contribution of higher-order dispersions has been neglected in deriving this expression. In the limit of $GDD \rightarrow 0$, the above GDD-dependent approximation of the pulse width breaks down, and the pulse width is instead determined by the higher-order dispersion coefficients (Supplementary Section 3.3). The pulse compression factor can then be expressed as T_p/τ_{sech} . We define a FOM that is indicative of the amount of pulse compression attained and can serve as a design guideline for achieving optimum soliton compression. The FOM in a non-zero GDD scenario for a given length (L) of the phase-matched quadratically nonlinear region is defined as (Supplementary Section 3)

$$\text{FOM} = \left| \frac{u^2 L}{\beta_2} \right|. \quad (1)$$

A large value of GVM and small value of GVD (β_2) (either normal or anomalous) favours efficient soliton compression. Figure 5a shows the experimental results of variation of the soliton spectral bandwidth with changing cavity dispersion that has been realized by combining different lengths of normal- and anomalous GVD fibres. Some of these fibre combinations yield net normal-cavity GVD (blue circles, Fig. 5a) and the rest experience net anomalous cavity GVD (green circle, Fig. 5a). The quadratic soliton can exist irrespective of the sign of the cavity second-order GVD coefficient. Extensive dispersion engineering capability can be accessed through an integrated nanophotonics platform that can be designed to maximize the FOM^{41,45,46}. Figure 5b presents a plot of the FOM as the width and etch depth of a typical lithium niobate ridge waveguide are varied (Supplementary Section 6). If we now consider a point corresponding to a large value of the FOM, we predict (using numerical simulation) a pulse compression in excess of a factor of 60 for a 6-mm-long parametric gain section (dispersion parameters are reported in Supplementary Section 6), leading to the generation of few optical-cycle pulses starting from picosecond pump pulses, as shown in Fig. 5c. Further improvement can be obtained by utilizing longer gain sections and engineering a flat dispersion profile while taking higher-order GVD coefficients into consideration (Supplementary Section 3.3)⁴⁷.

Discussion

Figure 6 presents an overview of the existing approaches to pulse compression in the parameter space of compression factor and pump pulse energy utilized. Prevailing popular approaches include, but are not limited to, pulse pumped Kerr solitons^{6,17}, Kerr solitons in enhancement cavities⁴⁸, Kerr solitons in active cavities³⁴, singly-resonant synchronously pumped OPOs⁴⁹ and soliton compression in waveguides^{50,51}. It is highly desirable to attain large compression factors with low pump pulse energy (top left corner of the landscape in Fig. 6). In our work, we have achieved a pump-to-signal pulse-compression factor of ~ 42 , which compressed an ~ 13.2 -ps flat-top pulse at 775 nm to ~ 316 fs at 1,550 nm, corresponding to a 3-dB spectral bandwidth of 8.3 nm (Supplementary Section 7). The pump average power was close to 1 mW, which amounts to 4 pJ of

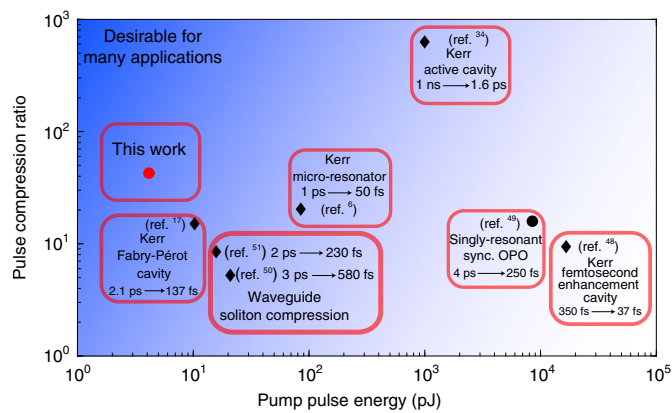


Fig. 6 | Comparison of existing approaches to quadratic and cubic nonlinearity-mediated pulse compression. The diamonds (Kerr nonlinearity-driven) and circles (quadratic nonlinearity-driven) indicate data points in the space of the amount of pulse compression attained against the average pump power used, as obtained from the indicated corresponding references. The desirable operating condition is located in the top left corner of the plot. Only pulse-driven systems have been considered here, and the c.w.-driven soliton generation process has not been included in this comparison.

pulse energy. This shows our work to be a marked advancement over existing approaches and elucidates the opportunities associated with soliton generation in quadratic nonlinear resonators. The experimental conversion efficiency is estimated to be near 10% (after considering the effect of insertion losses in the interfaces of the set-up), which is consistent with our numerical simulation (Supplementary Section 10). Additionally, extension of the demonstrated concept to integrated nanophotonic platforms will allow ultra-low-power operation with soliton formation possible at several femtojoules of pump pulse energy^{13,41,45}. The low-finesse operation relaxes fabrication requirements for on-chip realization of quadratic solitons, and the picosecond pump pulses can be generated using integrated electro-optic modulators⁵², thereby paving the way for complete system integration.

The dissipative quadratic soliton under consideration is reliant on pump pulses, which is unlike c.w.-driven Kerr solitons but shares similarities to other variants of solitons where a trigger pulse is required³⁴. However, the soliton exhibits only a weak dependence on the exact temporal structure of the pump pulse (Supplementary Section 12) because of the importance of all the balancing mechanisms for soliton formation.

We should also note that the presented soliton formation contrasts starkly with previous demonstrations of pulse compression in bulk OPOs, where only the non-degenerate signal oscillates^{40,49}. Although non-stationary OPA is a common element, the presented soliton formation in doubly-resonant OPOs is rooted in the interplay between phase-sensitive amplification and the degenerate signal resonant condition, which is absent in the singly-resonant counterparts. This demarcation is further accentuated by the synchronization of both the CEO frequency and the repetition rate to the pump, fixed output wavelength and low-power operation.

Various modes of operation of degenerate OPOs (DOPO) provide a rich landscape that can cater to the diverse requirements in ultra-short pulse sources in different wavelength ranges^{30,53}. The walk-off-induced soliton represents the giant pulse-compression regime of operation of DOPOs. In this solitonic regime, the pulse width scales with GDD, and good conversion efficiencies can be achieved on account of the low-finesse cavity operation. However, due to the gain-clipping-dominated box-pulse scaling behaviour, the bandwidth decreases with increasing pump power, which prevents

it from achieving even higher conversion efficiencies. The soliton regime represents another solitonic mode of operation of DOPOs³⁰. In this regime, GVD-free scaling of the pulse width is observed and, thanks to the favourable trend of increasing bandwidth with pump power, a higher conversion efficiency can be attained. However, the soliton regime requires that the detuning-induced timing mismatch and gain-clipping window have a comparable timescale along with some minimum third-order dispersion for its existence. This leads to a trade-off in terms of the attainable pulse compression and pump power (threshold requirement; Supplementary Section 11). Proper dispersion engineering of an OPO can lead to the formation of solitons in a dispersion regime where large pulse compression is expected to be accompanied by high (>50%) conversion efficiencies (Supplementary Section 11); this will be the subject of future work.

In summary, we have demonstrated the formation of walk-off-induced dissipative solitons in a DOPO. We have shown a substantial pulse-compression factor attainable with a picojoule-level pump, thanks to the strong quadratic nonlinearity. We have presented design guidelines for achieving efficient quadratic soliton formation in properly dispersion-engineered thin-film integrated devices^{45,52}. This holds promise for the generation of few-cycle pulses starting from easily accessible picosecond pump pulses, thereby paving the way for the realization of turn-key frequency-comb sources^{19,20}. In parallel to the ongoing efforts in relation to pure cubic and combined quadratic and cubic nonlinearities for soliton formation^{22,54,55}, our results highlight a route to realize solitons with pure quadratic nonlinearity with potential practical advantages in terms of conversion efficiency, wavelength diversity and cavity finesse requirements.

Online content

Any methods, additional references, Nature Research reporting summaries, source data, extended data, supplementary information, acknowledgements, peer review information; details of author contributions and competing interests; and statements of data and code availability are available at <https://doi.org/10.1038/s41566-021-00942-4>.

Received: 9 June 2021; Accepted: 1 December 2021;
Published online: 31 January 2022

References

- Kippenberg, T. J., Gaeta, A. L., Lipson, M. & Gorodetsky, M. L. Dissipative Kerr solitons in optical microresonators. *Science* **361**, eaan8083 (2018).
- Herr, T. et al. Temporal solitons in optical microresonators. *Nat. Photon.* **8**, 145–152 (2014).
- Dutt, A. et al. On-chip dual-comb source for spectroscopy. *Sci. Adv.* **4**, e1701858 (2018).
- Muraviev, A. V., Smolski, V. O., Loparo, Z. E. & Vodopyanov, K. L. Massively parallel sensing of trace molecules and their isotopologues with broadband subharmonic mid-infrared frequency combs. *Nat. Photon.* **12**, 209–214 (2018).
- Suh, M.-G. et al. Searching for exoplanets using a microresonator astrocomb. *Nat. Photon.* **13**, 25–30 (2019).
- Obrzud, E. et al. A microphotonic astrocomb. *Nat. Photon.* **13**, 31–35 (2019).
- Stern, L. et al. Direct Kerr frequency comb atomic spectroscopy and stabilization. *Sci. Adv.* **6**, eaax6230 (2020).
- Suh, M.-G. & Vahala, K. J. Soliton microcomb range measurement. *Science* **359**, 884–887 (2018).
- Trocha, P. et al. Ultrafast optical ranging using microresonator soliton frequency combs. *Science* **359**, 887–891 (2018).
- Ji, X. et al. Chip-based frequency comb sources for optical coherence tomography. *Opt. Express* **27**, 19896–19905 (2019).
- Marin-Palomo, P. et al. Microresonator-based solitons for massively parallel coherent optical communications. *Nature* **546**, 274–279 (2017).
- Xu, X. et al. 11 TOPS photonic convolutional accelerator for optical neural networks. *Nature* **589**, 44–51 (2021).
- Lu, J. et al. Ultralow-threshold thin-film lithium niobate optical parametric oscillator. *Optica* **8**, 539–544 (2021).

14. Xue, X., Zheng, X. & Zhou, B. Super-efficient temporal solitons in mutually coupled optical cavities. *Nat. Photon.* **13**, 616–622 (2019).
15. Xue, X., Wang, P.-H., Xuan, Y., Qi, M. & Weiner, A. M. Microresonator Kerr frequency combs with high conversion efficiency. *Laser Photon. Rev.* **11**, 1600276 (2017).
16. Bao, C. et al. Nonlinear conversion efficiency in Kerr frequency comb generation. *Opt. Lett.* **39**, 6126–6129 (2014).
17. Obrzud, E., Lecomte, S. & Herr, T. Temporal solitons in microresonators driven by optical pulses. *Nat. Photon.* **11**, 600–607 (2017).
18. Bao, H. et al. Laser cavity-soliton microcombs. *Nat. Photon.* **13**, 384–389 (2019).
19. Stern, B., Ji, X., Okawachi, Y., Gaeta, A. L. & Lipson, M. Battery-operated integrated frequency comb generator. *Nature* **562**, 401–405 (2018).
20. Shen, B. et al. Integrated turnkey soliton microcombs. *Nature* **582**, 365–369 (2020).
21. Moille, G. et al. Ultra-broadband Kerr microcomb through soliton spectral translation. *Nat. Commun.* **12**, 1–9.
22. Bruch, A. W. et al. Pockels soliton microcomb. *Nat. Photon.* **15**, 53–58 (2021).
23. Mosca, S. et al. Direct generation of optical frequency combs in $\chi^{(2)}$ nonlinear cavities. *Nanophotonics* **5**, 316–331 (2016).
24. Mosca, S. et al. Modulation instability induced frequency comb generation in a continuously pumped optical parametric oscillator. *Phys. Rev. Lett.* **121**, 093903 (2018).
25. Parra-Rivas, P., Gelens, L., Hansson, T., Wabnitz, S. & Leo, F. Frequency comb generation through the locking of domain walls in doubly resonant dispersive optical parametric oscillators. *Opt. Lett.* **44**, 2004–2007 (2019).
26. Leo, F. et al. Walk-off-induced modulation instability, temporal pattern formation, and frequency comb generation in cavity-enhanced second-harmonic generation. *Phys. Rev. Lett.* **116**, 033901 (2016).
27. Nie, M., Xie, Y. & Huang, S.-W. Deterministic generation of parametrically driven dissipative Kerr soliton. *Nanophotonics* **10**, 1691–1699 (2021).
28. Nie, M. & Huang, S.-W. Quadratic soliton mode-locked degenerate optical parametric oscillator. *Opt. Lett.* **45**, 2311–2314 (2020).
29. Leindecker, N. et al. Octave-spanning ultrafast OPO with 2.6–6.1- μm instantaneous bandwidth pumped by femtosecond Tm-fiber laser. *Opt. Express* **20**, 7046–7053 (2012).
30. Jankowski, M. et al. Temporal solitons in optical parametric oscillators. *Phys. Rev. Lett.* **120**, 053904 (2018).
31. Cole, D. C. et al. Kerr-microresonator solitons from a chirped background. *Optica* **5**, 1304–1310 (2018).
32. Jang, J. K., Erkintalo, M., Coen, S. & Murdoch, S. G. Temporal tweezing of light through the trapping and manipulation of temporal cavity solitons. *Nat. Commun.* **6**, 7370 (2015).
33. Erkintalo, M., Murdoch, S. G. & Coen, S. Phase and intensity control of dissipative Kerr cavity solitons. *J. R. Soc. New Zealand* <https://doi.org/10.1080/03036758.2021.1900296> (2021).
34. Englebert, N., Arabi, C. M., Parra-Rivas, P., Gorza, S.-P. & Leo, F. Temporal solitons in a coherently driven active resonator. *Nat. Photon* **15**, 536–541 (2021).
35. Akhmediev, N. & Ankiewicz, A. *Dissipative Solitons: from Optics to Biology and Medicine*, Vol. 751 (Springer Science & Business Media, 2008).
36. Hamerly, R. et al. Reduced models and design principles for half-harmonic generation in synchronously pumped optical parametric oscillators. *Phys. Rev. A* **94**, 063809 (2016).
37. Langrock, C. & Fejer, M. M. Fiber-feedback continuous-wave and synchronously-pumped singly-resonant ring optical parametric oscillators using reverse-proton-exchanged periodically-poled lithium niobate waveguides. *Opt. Lett.* **32**, 2263–2265 (2007).
38. Marandi, A., Langrock, C., Fejer, M. M. & Byer, R. L. Guided-wave half-harmonic generation of frequency combs with 75-fold spectral broadening. In *Proc. Nonlinear Optics*, NM1A-2 (Optical Society of America, 2015).
39. Akhmanov, S. et al. Nonstationary nonlinear optical effects and ultrashort light pulse formation. *IEEE J. Quantum Electron.* **4**, 598–605 (1968).
40. Khaydarov, J. D. V., Andrews, J. H. & Singer, K. D. Pulse-compression mechanism in a synchronously pumped optical parametric oscillator. *J. Opt. Soc. Am. B* **12**, 2199–2208 (1995).
41. Ledezma, L. et al. Intense optical parametric amplification in dispersion engineered nanophotonic lithium niobate waveguides. Preprint at <https://arxiv.org/abs/2104.08262> (2021).
42. Roy, A., Jahani, S., Langrock, C., Fejer, M. & Marandi, A. Spectral phase transitions in optical parametric oscillators. *Nat. Commun.* **12**, 835 (2021).
43. Gatti, A. & Lugiato, L. Quantum images and critical fluctuations in the optical parametric oscillator below threshold. *Phys. Rev. A* **52**, 1675–1690 (1995).
44. Trillo, S. Bright and dark solitons in second-harmonic generation. *Opt. Lett.* **21**, 1111–1113 (1996).
45. Jankowski, M. et al. Ultrabroadband nonlinear optics in nanophotonic periodically poled lithium niobate waveguides. *Optica* **7**, 40–46 (2020).
46. Jankowski, M. et al. Efficient octave-spanning parametric down-conversion at the picojoule level. Preprint at <https://arxiv.org/abs/2104.07928> (2021).
47. Dietrich, C. M. et al. Higher-order dispersion and the spectral behavior in a doubly resonant optical parametric oscillator. *Opt. Lett.* **45**, 5644–5647 (2020).
48. Lilienfein, N. et al. Temporal solitons in free-space femtosecond enhancement cavities. *Nat. Photon.* **13**, 214–218 (2019).
49. Lefort, L., Puech, K., Butterworth, S. D., Svirko, Y. P. & Hanna, D. C. Generation of femtosecond pulses from order-of-magnitude pulse compression in a synchronously pumped optical parametric oscillator based on periodically poled lithium niobate. *Opt. Lett.* **24**, 28–30 (1999).
50. Colman, P. et al. Temporal solitons and pulse compression in photonic crystal waveguides. *Nat. Photon.* **4**, 862–868 (2010).
51. Choi, J. W., Sohn, B.-U., Chen, G. F. R., Ng, D. K. T. & Tan, D. T. H. Soliton-effect optical pulse compression in CMOS-compatible ultra-silicon-rich nitride waveguides. *APL Photonics* **4**, 110804 (2019).
52. Wang, C., Zhang, M., Stern, B., Lipson, M. & Lončar, M. Nanophotonic lithium niobate electro-optic modulators. *Opt. Express* **26**, 1547–1555 (2018).
53. Ru, Q. et al. Self-referenced octave-wide subharmonic GaP optical parametric oscillator centered at 3 μm and pumped by an Er-fiber laser. *Opt. Lett.* **42**, 4756–4759 (2017).
54. Englebert, N. et al. Parametrically driven Kerr cavity solitons. *Nat. Photon.* **15**, 857–861 (2021).
55. O'Donnell, C. F., Kumar, S. C., Paoletta, T. & Ebrahim-Zadeh, M. Widely tunable femtosecond soliton generation in a fiber-feedback optical parametric oscillator. *Optica* **7**, 426–433 (2020).

Publisher's note Springer Nature remains neutral with regard to jurisdictional claims in published maps and institutional affiliations.

© The Author(s), under exclusive licence to Springer Nature Limited 2022

Methods

Experimental set-up. A simplified experimental schematic is shown in Fig. 1a, a detailed version of which is presented as Supplementary Fig. 1 (Supplementary Section 2). The OPO pump is derived from the mode-locked laser through second-harmonic generation in a 40-mm-long bulk quasi-phase-matched periodically poled lithium niobate (PPLN) crystal. The pump is centred around 775 nm, a value that can be thermally tuned, and is ~13 ps in duration. This provides approximately the optimum pump length for soliton formation, because it satisfies $T_p = Lu$. The main cavity is composed of a PPLN waveguide (reverse proton exchange, 40 mm long)³⁷ with fibre-coupled output ports, fibre phase shifter, free-space section (to adjust the pump repetition rate to be a multiple of the free spectral range of the cavity; the cavity consists of three or four pulses per roundtrip depending on the length of the fibre combinations used), an additional fibre segment to engineer the cavity dispersion (combination of a polarization-maintaining single mode providing anomalous dispersion and dispersion-compensating fibres providing normal dispersion) and a beamsplitter, which provides the output coupling. The cavity length is stabilized using the Pound–Drever–Hall (PDH) locking scheme. It should be noted that the PDH locking scheme employed in the experiment is used to prevent the slow drift only and does not play a role in the timing balance or synchronization process. The temporal characterizations of the pulses are obtained using the non-collinear sum-frequency generation cross-correlation technique in a beta barium borate crystal. Additional details pertaining to the experimental set-up and methods are provided in Supplementary Section 2.

System modelling. The quadratic nonlinear interaction inside the PPLN waveguide (length L) is governed by

$$\frac{\partial a}{\partial z} = \left[-\frac{\alpha^{(a)}}{2} - i\frac{\beta_2^{(a)}}{2!} \frac{\partial^2}{\partial t^2} + \dots \right] a + \epsilon a^* b \quad (2a)$$

$$\frac{\partial b}{\partial z} = \left[-\frac{\alpha^{(b)}}{2} - u \frac{\partial}{\partial t} - i\frac{\beta_2^{(b)}}{2!} \frac{\partial^2}{\partial t^2} + \dots \right] b - \frac{\epsilon a^2}{2} \quad (2b)$$

The evolutions of the signal (a) and pump (b) envelopes in the slowly varying envelope approximation are dictated by equations (2a) and (2b), respectively³⁶. Here, $*$ denotes complex conjugation, u represents the walk-off parameter, α denotes the loss coefficients and the GVD coefficients are denoted by β . The effective second-order nonlinear coefficient (ϵ) is related to the second-harmonic generation efficiency³⁶. The roundtrip cavity feedback (outside the periodically poled region) is given by

$$a^{(n+1)}(0, t) = \mathcal{F}^{-1} \left\{ G_0^{-\frac{1}{2}} e^{i\bar{\phi}} \mathcal{F} \left\{ a^{(n)}(L, t) \right\} \right\} \quad (3a)$$

$$\bar{\phi} = \Delta\phi + \frac{l\lambda^{(a)}}{2c}(\delta\omega) + \frac{\phi_2}{2!}(\delta\omega)^2 + \dots \quad (3b)$$

Equations (3a) and (3b) take into consideration the roundtrip loss, which is lumped into an aggregated outcoupling loss factor G_0 , the GVD (ϕ_2) of the feedback path and the detuning ($\Delta\phi$) ($\Delta\phi = \pi l$, where l is the cavity length detuning in units of signal half-wavelengths in vacuum) of the circulating signal from the exact synchrony with respect to the periodic pump. The roundtrip

number is denoted by n . The fast time represents the timescale within a roundtrip. The equations are numerically solved adopting the split-step Fourier algorithm. Further details are provided in Supplementary Sections 3 and 4. We also adopted the manifold projection method to obtain semi-analytical expression of the soliton parameters. Results obtained in this approach are referred to as analytical. The sech profile is considered as an approximation to the pulse shape in the soliton regime and has been used as an ansatz for the semi-analytical variational calculations.

The optical spectrum shown in Fig. 3a,b deviates from the sech² shape and closely resembles a Gaussian profile, a feature that has been observed in the context of stretched solitons^{56,57}. This is the case in our experimental implementation, where low values of cavity GDD have been realized utilizing appropriate lengths of both normal and anomalous dispersion fibres. This scenario will not appear in the case of uniformly dispersion-engineered cavities designed on an integrated platform, where the sech profile can be a good approximation to the soliton pulse shape.

Data availability

The data that support the plots within this paper are available at <https://doi.org/10.6084/m9.figshare.17040335>.

Code availability

The codes that support the findings of this study are available from the corresponding author upon reasonable request.

References

- Dong, X., Yang, Q., Spiess, C., Bucklew, V. G. & Renninger, W. H. Stretched-pulse soliton Kerr resonators. *Phys. Rev. Lett.* **125**, 033902 (2020).
- Chen, Y. et al. Dispersion-managed mode locking. *J. Opt. Soc. Am. B* **16**, 1999–2004 (1999).

Acknowledgements

We acknowledge support from AFOSR award no. FA9550-20-1-0040 (to A.M.), NSF grant no. 1846273 (to A.M.) and NASA (to A.M.). We also thank NTT Research for their financial and technical support. We thank R. Gray for his valuable input.

Author contributions

A.R. performed the experiments with help from R.N. A.R. and L.L. developed the theory and performed the numerical simulations. C.L. fabricated the PPLN waveguide used in the experiment, with supervision from M.F. All authors contributed to analysis of the results. A.R. and A.M. wrote the manuscript with input from all authors. A.M. supervised the project.

Competing interests

The authors declare no competing interests.

Additional information

Supplementary information The online version contains supplementary material available at <https://doi.org/10.1038/s41566-021-00942-4>.

Correspondence and requests for materials should be addressed to Alireza Marandi.

Peer review information *Nature Nanotechnology* thanks the anonymous reviewers for their contribution to the peer review of this work.

Reprints and permissions information is available at www.nature.com/reprints.